Green Chemistry

PAPER

View Article Online
View Journal | View Issue

Cite this: *Green Chem.*, 2025, **27**, 7368

Chemical looping hydrogen production from ammonia and water: materials and technoeconomics†

Amirmohammad Arjomand Kermani,[a] Kyle Shank[a] and Shang Zhai *[a,b]

Received 15th January 2025,
Accepted 21st May 2025

DOI: 10.1039/d5gc00236b

rsc.li/greenchem

Ammonia (NH_3) is a promising hydrogen carrier due to high hydrogen density and established infrastructure. We present a novel chemical looping process to produce H_2 from NH_3 oxidation and decomposition and from water splitting, integrating thermochemical redox looping and catalytic reaction. Unlike single-step catalytic NH_3 decomposition, the looping configuration produces high purity H_2 from the water splitting that significantly lowers separation energy and cost. FeO_x/YSZ and $Fe_{0.5}Co_{0.5}O_x$/YSZ were shown as durable dual-functional oxygen carriers and catalysts, achieving 95% and 99% NH_3 conversion and 39% and 25% water splitting conversion, respectively. The materials' redox capacities were explained by simultaneous Fe and Co redox reactions and solid-state phase transition between metal (alloy) and spinel. From 450 to 600 °C, Fe redox capacity increased, while Co redox capacity decreased. Kinetic limitations hindered full reduction of FeO_x/YSZ to metallic Fe at 450 °C due to lack of the effective Co catalyst, while thermodynamic limitations prevented complete oxidation of Co metal in $Fe_{0.5}Co_{0.5}O_x$/YSZ. Techno-economic analysis showed the looping process achieves 52% to 86% lower energy and equipment costs than single-step catalytic NH_3 decomposition with different H_2 separation methods.

Green foundation

1. This paper presents a novel process of chemical looping ammonia oxidation and decomposition integrated with water splitting (CLAOD-WS). Compared to single-step catalytic NH_3 decomposition, CLAOD-WS gives high purity H_2 to significantly lower separation energy and cost, enabling NH_3 as a promising hydrogen carrier.
2. FeO_x/YSZ and $Fe_{0.5}Co_{0.5}O_x$/YSZ were shown as durable dual-functional oxygen carriers and catalysts. The materials' redox capacities were explained by simultaneous Fe and Co redox reactions and solid-state phase transition between metal (alloy) and spinel. The looping process achieves 52% to 86% lower energy and equipment costs than single-step catalytic NH_3 decomposition.
3. Future research can include reactor design and materials chemistry to co-optimize oxygen exchange capacity and catalytic reactivity, so that almost all H_2 is produced from water splitting step rather than NH_3 conversion step, further lowing H_2 separation energy and cost.

1. Introduction

Addressing the Gigaton-scale greenhouse gas (GHG) emissions challenge is critical for mitigating global warming.[1] Clean hydrogen (H_2) produced without GHG emissions offers significant potential to support carbon neutrality, especially in hard-to-decarbonize sectors including industry and transportation.[2,3] Its applications span chemical feedstock, steel production, fuel for heavy-duty transport, industrial/domestic heating, and renewable energy storage.[2,3] To expand clean H_2 utilization, the issue of energy-intensive and costly H_2 delivery needs to be overcome.[1,4] The current cost to produce GHG-free H_2 with water electrolysis is about $4–5 per kg,[5] while the average cost of transporting and dispensing H_2 can range from $8.17–$9.46 per kg for gaseous tube trailers and $8.31–$11.35 per kg for liquid tankers,[6] mainly because H_2 compression and liquefaction are expensive and energy-intensive.[7–11] Chemical hydrogen carriers have the potential to help lower energy demand and cost for H_2 delivery.[1,4,12]

NH_3 proves to be an excellent hydrogen carrier. Firstly, it possesses a high volumetric and gravimetric hydrogen density compared to several well-known hydrogen carriers (Fig. 1a).[1,12,13] At 298 K and 1 MPa, the volumetric hydrogen density of NH_3 is

[a]*Department of Mechanical and Aerospace Engineering, The Ohio State University, 201 West 19th Ave, Columbus, OH 43210, USA. E-mail: zhai.218@osu.edu*
[b]*School of Earth Sciences, The Ohio State University, 125 South Oval Mall, Columbus, OH 43210, USA*

†Electronic supplementary information (ESI) available: Experimental methods, data analysis methods and results, additional looping performance data, equilibrium simulation method, energy and technoeconomic analysis methods. See DOI: https://doi.org/10.1039/d5gc00236b

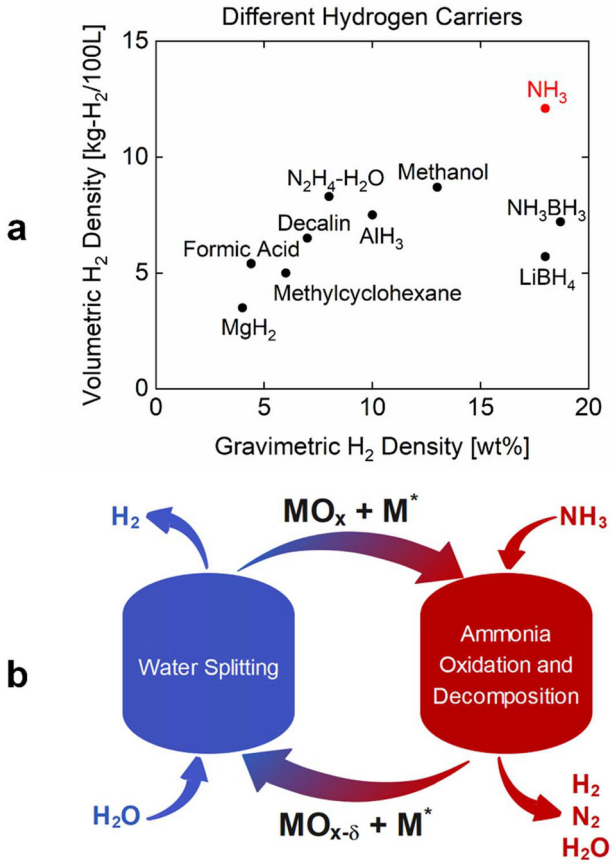

Fig. 1 (a) Comparison among chemical hydrogen carriers for volumetric and gravimetric hydrogen densities at 0.1 MPa and 240 K. Adapted from references.[1,12,13,17–20] (b) Chemical looping ammonia oxidation and decomposition integrated with water splitting (CLAOD-WS) process schematic. MO_x is a redox active metal oxide, and M* is a metallic catalyst. Compositions of M and M* may change between the reduced and oxidized states.

60 times that of H_2, and the storage cost of NH_3 is only 3% of H_2.[1] Secondly, NH_3 is vastly utilized as a fertilizer in agriculture; consequently, well-established infrastructure exists in many countries.[14] NH_3 has been easily and safely transported *via* pipelines, trucks, and rail cargos for many decades.[1,15,16]

Catalytic NH_3 decomposition to H_2 has been extensively studied and catalysts such as noble metals of ruthenium (Ru) and platinum (Pt) or transition metal-based catalysts of nickel (Ni), cobalt (Co), and iron (Fe) have been investigated to give high conversions (>95%) at moderate temperatures (450–600 °C).[4,21–24] In a study on noble metal catalysts by Yao *et al.*, high NH_3 conversion of 96% was achieved at the moderate temperature of 500 °C using nanoparticles of Ru on silica (SiO_2) support.[24] In a comprehensive study by Gu *et al.*, Co, Ni, and Fe were synthesized on alumina (Al_2O_3) support, with catalytic NH_3 decomposition at 600 °C revealing conversion rates of 100%, 93%, and 86% for Co, Ni, and Fe catalysts, respectively.[23] Xie *et al.* tuned CoMoFeNiCu high entropy alloy catalyst nanoparticles dispersed on carbon nanofibers which reached 100% conversion of NH_3 at 525 °C for $Co_{25}Mo_{45}Fe_{10}Ni_{10}Cu_{10}$. This was compared to bimetallic Co–Mo and monometallic Ru which only reached 46% and 73% conversion, respectively, at 600 °C.[22] Tabassum *et al.* present a Ru-free catalyst composed of a CoNi alloy supported on a K-promoted MgO–CeO_2–SrO mixed oxide, achieving nearly complete NH_3 conversion at 450 °C. The catalyst demonstrates high stability and hydrogen production rates comparable to Ru-based catalysts, highlighting the role of metal–oxide interfaces and promoter effects in enhancing activity and stability.[21]

Oxygen carrier metal oxides have been researched for NH_3 oxidation to nitrogen (N_2) and nitrogen oxides (NO_x). Normann *et al.* introduced a chemical looping scheme in which NH_3 was oxidized using Fe, manganese (Mn), and Ni-based oxygen carriers; afterwards, the oxygen carriers were re-oxidized by oxygen.[25] This work focused on the production of nitric oxide (NO) and H_2O from NH_3 oxidation and concluded that Mn-based oxide demonstrates the best performance in NO formation. In another study, Cheng *et al.* investigated NH_3 oxidation to NO_x and N_2 using Ilmenite (iron–titanium oxide).[26] It was discovered that decreasing NH_3 concentration decreases the selectivity of NH_3 decomposition toward N_2 and increases that toward NO formation. Ruan *et al.* investigated a chemical looping scheme in which NH_3 was selectively oxidized to form NO using a vanadium pentoxide (V_2O_5) oxygen carrier and then the oxygen carrier was re-oxidized using oxygen gas (O_2).[27] This configuration achieved over 95% NH_3 conversion and 100% NO selectivity at 650 °C.

Oxygen carriers have also been studied in thermochemical redox cycles for H_2 production by water splitting.[28–43] The oxygen capacity of the carrier materials comes from either solid phase transformation or oxygen vacancy. One category of the redox cycles uses high temperature to thermally reduce the oxygen carrier. Zhai *et al.* utilized mixed metal oxides called poly-cation oxides (PCOs) which consist of transition metals Fe, Mg, Co, and Ni. Fe redox in the PCOs provided the redox capacity, while the other redox inactive metals helped tune the oxide phase transformation to lower the reduction reaction temperature for a lower system cost.[28] Tran *et al.* examined the performance of iron aluminate ($(Fe_{0.33}Al_{0.67})_{3-\delta}O_4$) for H_2O and CO_2 splitting reactions. Thermal reduction at 1400 °C was followed by oxidation at elevated pressures (1–10 atm), resulting in enhanced equilibrium extent and reaction kinetics.[38] Wexler *et al.* presented a newly developed perovskite material, $Ca_{2/3}Ce_{1/3}Ti_{1/3}Mn_{2/3}O_3$, which exhibits high hydrogen production capacity and stable redox performance. The authors identified that the A-site Ce^{4+} reduction is the key to its enhanced water splitting capabilities.[43] Tran *et al.* reviewed the potential of perovskite oxides as redox materials for CO_2 splitting using solar thermochemical methods. This work highlights their lower reduction temperatures, tunable properties, and challenges such as sintering and cycle stability for solar-driven fuel production.[44] The other category of redox cycles uses chemical reduction for the oxygen carrier. We refer to review articles and book in this area.[45–47]

Building on the previous work, we present chemical looping ammonia oxidation and decomposition integrated with water

splitting (CLAOD-WS), a novel two-step cyclic process involving redox looping and catalytic reactions for H_2 production from NH_3 and H_2O (Fig. 1b). Here NH_3 is first partially oxidized by a solid oxygen carrier and meanwhile decomposed by a catalyst, to produce H_2, N_2, and H_2O (eqn (1)); secondly, H_2O re-oxidizes the oxygen carrier to produce H_2 (eqn (2)).

$$NH_3 + MO_x \rightarrow \left(\frac{3}{2} - \delta\right)H_2 + \frac{1}{2}N_2 + \delta H_2O + MO_{x-\delta} \quad (1)$$

$$\delta H_2O + MO_{x-\delta} \rightarrow \delta H_2 + MO_x \quad (2)$$

Over CLAOD-WS cycles, the net reaction is the same as NH_3 decomposition producing N_2 and H_2, but looping presents advantages that will translate to significant energy and cost savings shown by this paper. Firstly, it gives two H_2 streams at different purity levels suitable for different applications. On the one hand, the H_2 produced by water splitting step is intrinsically separated from N_2 and NH_3. This H_2 has only unreacted H_2O as impurity and is thus more suitable for high-purity H_2 applications such as fuel cells.[48–50] If necessary, this stream of H_2 mixed with unreacted H_2O can be further purified by removing H_2O, which is simpler than H_2 separation from N_2 and unreacted NH_3 in direct NH_3 decomposition. On the other hand, the low-purity H_2 from the NH_3 conversion step is mixed with N_2, H_2O, and unreacted NH_3, and can be suitable for industrial heating and power generation. Secondly, according to Le Chatelier's principle, chemical looping facilitates NH_3 conversion thanks to the removal of H_2 by the chemical reduction of the oxygen carrier.

Previous literature on system energy and technoeconomic assessments provides information for our analysis of CLAOD-WS in comparison to direct NH_3 decomposition in terms of energy consumption, H_2 production, and process costs. Yun *et al.* analyzed catalytic NH_3 decomposition plants equipped with various types of H_2 separation systems including pressure swing absorption (PSA) and Pd membranes, where the levelized cost of H_2 (LCOH) was reported between \$5–7.5 per kg-H_2.[51] Nordio *et al.* proposed a H_2 separation system integrated with multiple membrane modules and conducted a comprehensive technoeconomic analysis. This study concluded that LCOH ranges between €3.56 and €12.63 per kg-H_2.[52] Makhloufi *et al.* studied a large-scale NH_3 cracking system for clean H_2 production. This plant showed 68.5% thermal efficiency and €4.83 per kg-H_2.[53] In another study by Devkota *et al.*, technoeconomic and environmental assessment of an NH_3 decomposition plant equipped with a packed bed reactor concluded that LCOH was \$6.05 per kg-H_2.[54]

This study leverages catalytic and redox activities of FeO_x/YSZ and $Fe_{0.5}Co_{0.5}O_x$/YSZ for CLAOD-WS. We identified the different redox and catalytic properties of Fe and Co. Also, we showed that kinetic limitation and thermodynamic limitation occurred for different materials under different reaction conditions. Stable 50-cycle operation at 600 °C showed the materials' durability. Our energy and technoeconomic analyses compared CLAOD-WS with direct catalytic NH_3 decomposition systems.

2. Materials and methods

2.1. YSZ supported materials synthesis

Iron oxide and mixed iron–cobalt oxide were synthesized using a modified wet impregnation method. For the iron oxide, $Fe(NO_3)_3{\cdot}9H_2O$ (Sigma-Aldrich) was mixed with ethanol, and 8% yttria-stabilized zirconia (YSZ8%) ($(ZrO_2)_{0.92}(Y_2O_3)_{0.08}$) (Inframat Advanced Materials) was supplemented to the mixture as the oxygen carrier's support material. The mass of the support material was calculated to be 30% of the total mass of metal oxide and support. The mixture was stirred on a hotplate at 300 rpm for three hours at ambient temperature, followed by heating to 100 °C and stirring for two more hours. At this point, a thick paste was formed which was moved to a box furnace (MTI KSL-1200X) and dried at 200 °C for seven hours (heating and cooling ramp rates were 5 °C min^{-1}). The resulting dry material was ground with a mortar and pestle to obtain a fine powder. Lastly, calcination was carried out under air at 600 °C for three hours (heating and cooling ramp rates were 15 and 5 °C min^{-1} respectively) in the box furnace. The final product was further ground by mortar and pestle. This sample is denoted as FeO_x/YSZ. For the mixed iron–cobalt oxide, $Fe(NO_3)_3{\cdot}9H_2O$ and $Co(NO_3)_2{\cdot}6H_2O$ (Sigma-Aldrich) were mixed with the support following the same procedure. This sample is denoted as $Fe_{0.5}Co_{0.5}O_x$/YSZ.

2.2. Materials looping performance testing

CLAOD-WS experiments were conducted in a U-shaped quartz tube (O.D. = 0.5 in) in a Micromeritics tube furnace. 0.01 g material was uniformly placed inside the tube between quartz wool to form a fixed bed reactor. The reactor was programmed for isothermal reaction temperatures of 450, 500, 550, and 600 °C, with a 15 °C min^{-1} ramp rate, and three different space velocity values of 6, 18, and 30 L_{NH_3} $(g_{solid}\ h)^{-1}$. During heating up, 100 sccm of argon (Ar) flowed over the sample. At the determined reaction temperature, the first step began by flowing NH_3 gas balanced with Ar for 12 minutes unless otherwise noted, and consequently, H_2, N_2, and H_2O were produced. Different concentrations of NH_3 (1%, 3%, and 5%) were chosen for space velocities of 6, 18, and 30 L_{NH_3} $(g_{solid}\ h)^{-1}$, respectively (eqn (S1)†). In the second step, 2% H_2O vapor diluted in Ar flowed over the reduced material for 3 minutes unless otherwise noted; H_2O step space velocity was equal to 12 L_{H_2O} $(g_{solid}\ h)^{-1}$ in all experiments (eqn (S2)†). After each step, 100 sccm of Ar flowed for 5 minutes to purge the reactor and gas lines. A mass spectrometer (Hiden Analytical HPR-20 R&D) and gas chromatograph (Inficon Micro GC Fusion) were used in parallel to detect and quantify the gas mixture in the exhaust line. Potential NO_x was detected at a small amount in the NH_3 step of the first CLAOD-WS cycle for several samples, and no NO_x was detected beyond the first cycle (Fig. S4†).

2.3. Material characterization using XRD

X-ray diffraction (XRD) characterizations were performed using a Rigaku SmartLab X-ray diffractometer at ambient pressure and temperature. The data collection range was 2θ from 20° to 90°

with a 0.02° step size and 1.3° min^{-1} rate. XRD measurements were conducted on NH_3-reduced and steam-oxidized samples. To prepare the NH_3-reduced samples, 0.07 g material was reduced by NH_3 gas for 60 minutes and was carefully protected in a glove box filled with Ar due to their sensitivity to air. To prepare the steam-oxidized samples, the material was first reduced by NH_3 for 60 minutes and then re-oxidized by H_2O for 30 minutes and protected in Ar glove box. To keep the sample shielded from air oxidation, Kapton tape was used to protect the samples when taking the sample from the glove box to diffractometer.

We used 0.07 g sample for XRD and XANES measurements rather than the 0.01 g used for looping performance experiments because 0.01 g sample gave too low signal-to-noise ratio in the characterization results. Also, the 60-minute duration of the reduction step gave stable concentrations of products (N_2 and H_2) for at least 10 minutes in the NH_3 step, meaning the reduction of oxygen carrier was completed and the gas products were exclusively from NH_3 decomposition. Similarly, the 30-minute duration of the re-oxidation step gave zero H_2 product concentration for at least 10 minutes so that steam oxidation of the oxygen carrier was completed.

Refinement and Reference Intensity Ratio (RIR) methods in PDXL software were used to analyze the XRD data to quantify the phase compositions. Using chemical stoichiometry and molar mass of different solid phases, the molar ratio of oxygen to Fe plus Co can be calculated for each material at reduced and re-oxidized states. The difference in this ratio between reduced and re-oxidized samples shows the sample's oxygen exchange capacity normalized by the redox active metals (Fe and Co) molar amount (eqn (3)).

$$\Delta\left(\frac{\text{mol O}}{\text{mol M}}\right) = \left(\frac{\text{mol O}}{\text{mol M}}\right)_{\text{oxidized}} - \left(\frac{\text{mol O}}{\text{mol M}}\right)_{\text{reduced}} \quad (3)$$

2.4. Material characterization using XANES

X-ray absorption near edge structure (XANES) was conducted by easyXAFS300+ to measure the change in the oxidation state of the Fe and Co. The X-ray source was set at 36 kV and 20 mA to acquire energy absorption spectra ranging from 7000 eV to 7600 eV for Fe K edge and from 7600 eV to 7900 eV for Co K edge. NH_3-reduced and steam-oxidized samples (FeO_x/YSZ and $Fe_{0.5}Co_{0.5}O_x$/YSZ) and standard materials (Co, CoO, Co_3O_4, Fe, Fe_3O_4, and $CoFe_2O_4$) were protected against air oxidation using Kapton tape. FeO_x/YSZ and $Fe_{0.5}Co_{0.5}O_x$/YSZ samples were prepared in the same way as XRD samples. X-ray energy value at 0.5 normalized absorption was defined as the edge energy, and the edge energy of the reduced and re-oxidized samples relative to standard materials allowed us to determine the average oxidation states of Fe and Co in our samples. XANES data was analyzed by Athena software to give normalized absorption (μ) *vs.* absorption energy.[55]

2.5. Material characterization using SEM

Scanning Electron Microscopy (SEM) images were acquired using the Everhart–Thornley Detector (ETD) of a Thermo Fisher Scientific Apreo Scanning Electron Microscope set at 5 kV and 3.2 nA in the Secondary Electron (SE) mode. As-synthesized or cycled FeO_x/YSZ and $Fe_{0.5}Co_{0.5}O_x$/YSZ were mixed in deionized water and sonicated at ambient temperature (25 °C) for 5 minutes, a 10 μL droplet of the mixture was placed on an SEM stub covered with carbon tape; afterwards, the stub was dried for 5 hours at 80 °C on a hot plate to remove water.

3. Results and discussion

We conducted five-cycle CLAOD-WS experiments using 0.01 g FeO_x/YSZ or $Fe_{0.5}Co_{0.5}O_x$/YSZ at 450, 500, 550, and 600 °C. Fig. 2a shows reactor outlet gas mixture profile during a 600 °C experiment using FeO_x/YSZ at 6 L_{NH_3} $(g_{solid}\ h)^{-1}$. Initially, NH_3 was mostly oxidized into H_2O, and then when oxygen carrier capacity was used up, NH_3 was only catalytically

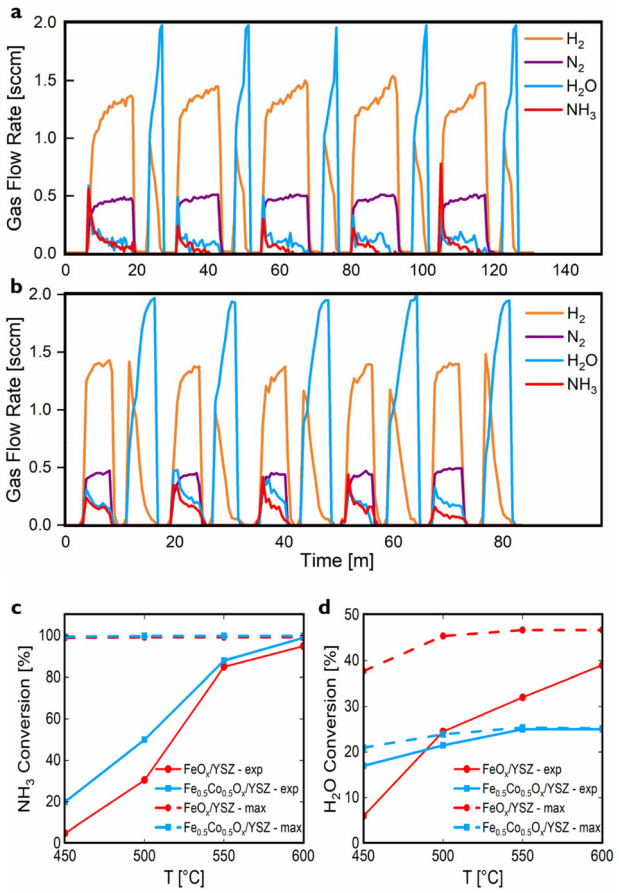

Fig. 2 CLAOD-WS performance for different materials at different temperatures. Reactor outlet gas profiles using FeO_x/YSZ at 600 °C with different step durations of (a) Δt_{NH_3} = 12 min and Δt_{H_2O} = 3 min, and (b) Δt_{NH_3} = 5 min and Δt_{H_2O} = 5 min. (c) NH_3 and (d) H_2O conversions dependence on temperature for $Fe_{0.5}Co_{0.5}O_x$/YSZ and FeO_x/YSZ. "max" refers to equilibrium and "exp" refers to average over five-cycle CLAOD-WS experiments. Experiments in (a–d) had space velocities 6 L_{NH_3} $(g_{solid}\ h)^{-1}$ and 12 L_{H_2O} $(g_{solid}\ h)^{-1}$.

decomposed to H_2 and N_2. In water splitting, H_2O re-oxidizes the oxygen carrier to produce additional H_2 until the re-oxidation is complete.

Space velocities and step durations can be adjusted to regulate the relative ratio of H_2 produced from the two steps. As in Fig. 2a, the ratio of H_2 from the NH_3 and H_2O steps was 7.43 : 1, while in Fig. 2b with shorter NH_3 step and longer H_2O step, this ratio became 2.13 : 1. Future research can involve materials chemistry adjustments and process optimizations to enhance high-purity H_2 production from H_2O in the CLAOD-WS system. Also, increasing the space velocity of the NH_3 step from 6 to 30 L_{NH_3} $(g_{solid}\ h)^{-1}$ only led to minor decay in NH_3 conversion from 99% to 95% for $Fe_{0.5}Co_{0.5}O_x$/YSZ and from 95% to 84% for FeO_x/YSZ at 600 °C (Fig. S1 and S2†). Therefore, sufficiently high conversions were achieved at space velocities suitable for commercial use conditions (≥7.8 L_{NH_3} $(g_{solid}\ h)^{-1}$).[56]

Experimental results from different temperatures are demonstrated in Fig. 2c, d, S1, and S2.† The solid lines indicate experimental results in Fig. 2c and d, while the dashed lines show thermodynamic equilibrium simulation results *via* FactSage software, giving the maximum possible conversions of NH_3 and H_2O. Fig. 2c shows an increasing trend in experimental NH_3 conversion as the temperature increases due to kinetics enhancement. Meanwhile, water splitting is improved at higher temperatures (Fig. 2d), specifically in FeO_x/YSZ, because both reaction kinetics and equilibrium H_2O conversion are improved at elevated temperatures.

To measure the materials' durability, 50-cycle CLAOD-WS were conducted at 600 °C and 30 L_{NH_3} $(g_{solid}\ h)^{-1}$ space velocity, the most demanding reaction condition in this paper. Over the 50 cycles, FeO_x/YSZ had only slight decays of 1.3% and 0.9% in NH_3 and H_2O conversions, respectively (Fig. 3a). Similarly, in Fig. 3d, $Fe_{0.5}Co_{0.5}O_x$/YSZ gave slight decays of 1.6% and 0.6% in NH_3 and H_2O conversions, respectively. Scanning electron microscope (SEM), showed surface topology and particle size did not change after the 50-cycle experiments (Fig. 3b–f), indicating negligible agglomeration and sintering. Stability assessment of these materials in commercial reactors requires longer duration which is out of the scope of this study.

Fig. 3g compares H_2 yield from NH_3 between chemical looping (only counting H_2 from the NH_3 step) and catalytic NH_3 decomposition in literature. The looping scheme shows high H_2 yields from the NH_3 at a range of space velocities. Fig. 3h compares thermochemical water splitting in literature with our CLAOD-WS experiments in millimoles H_2 production from H_2O per gram of oxygen carrier (OC). FeO_x/YSZ and $Fe_{0.5}Co_{0.5}O_x$/YSZ are among the best-performing water splitting oxygen carriers.

Other oxygen carriers and catalysts FeO_x/Al_2O_3, $Fe_{0.5}Co_{0.5}O_x/Al_2O_3$, CoO_x/YSZ, NiO_x/YSZ, and $Fe_{0.5}Ni_{0.5}O_x$/YSZ were also synthesized and tested for CLAOD-WS (Fig. S3 and Table S1†). We found that Al_2O_3 is not as effective a support as YSZ. Also, Co and Ni both showed minimal water splitting performance due to limited redox capacity. Additionally, Co is a better NH_3 conversion catalyst than Ni.

Material solid-phase transformation was studied by X-ray diffraction. At 450 °C, $Fe_{0.5}Co_{0.5}O_x$/YSZ was fully reduced by NH_3 to iron–cobalt metallic alloy (Fig. 4a), and then oxidized by H_2O to spinel phase while a portion of Co remained metallic (Fig. 4b), so the steam oxidation limited the redox capacity. With the same reaction conditions, FeO_x/YSZ was partially reduced by NH_3 to metallic iron with a spinel oxide phase remaining (Fig. 4c), and then oxidized by H_2O to complete spinel (Fig. 4d), so the reduction reaction limited the redox capacity. At 600 °C, FeO_x/YSZ was fully reduced by NH_3 to metallic Fe (Fig. 4g); and then fully oxidized by H_2O to spinel (Fig. 4h), giving complete phase transformation and thus high redox capacity. However, the $Fe_{0.5}Co_{0.5}O_x$/YSZ exhibited full reduction to metallic phase but still partial oxidation to spinel phase at 600 °C (Fig. 4e and f), similar to its behavior at 450 °C. Therefore, the elevated temperature more significantly enhanced the redox phase transformation of FeO_x/YSZ than $Fe_{0.5}Co_{0.5}O_x$/YSZ, explaining their looping performance trend in Fig. 2d. Kapton tape was used to minimize XRD samples' oxidation by air, so amorphous peaks at 2θ of 20° to 30° showed up.

The red arrows in Fig. 4i and j indicate the phase transition range at equilibrium conditions of NH_3 reduction and H_2O re-oxidation steps. For Fe–O system, at lower temperatures, the equilibrium phase transition is directly from Fe to Fe_3O_4, whereas at 600 °C the phase transition becomes Fe → FeO → Fe_3O_4. Fig. 4c showed that FeO_x/YSZ was not fully reduced by NH_3 to the metallic phase at 450 °C. Therefore, kinetic limitation prevented FeO_x/YSZ from achieving a fully reduced state at 450 °C. For the Fe–Co–O system, after oxidation at both temperatures, a portion of Co remains in the metallic phase due to thermodynamic limitation, consistent with XRD results. Therefore, thermodynamic limitation prevents metallic Co from being completely oxidized by H_2O and thus limits the redox capacity of $Fe_{0.5}Co_{0.5}O_x$/YSZ compared to FeO_x/YSZ.

By XRD refinement, the oxygen-to-metal molar ratios were calculated for 450 °C and 600 °C looping, and are shown in Fig. 4k. At 450 °C, owing to the full reduction of $Fe_{0.5}Co_{0.5}O_x$/YSZ and its oxidation to mostly spinel phase, the redox capacity of $Fe_{0.5}Co_{0.5}O_x$/YSZ is significantly higher than that of FeO_x/YSZ. At 600 °C, full reduction of FeO_x/YSZ to metallic phase followed by full oxidation to spinel phase resulted in its higher oxygen capacity than $Fe_{0.5}Co_{0.5}O_x$/YSZ. These are consistent with their water splitting capacity performance (Fig. 2d). The redox capacity of $Fe_{0.5}Co_{0.5}O_x$/YSZ is not significantly different between 450 °C and 600 °C based on XRD refinement, so X-ray Absorption Near Edge Structure (XANES) was utilized to further interpret each element's redox behavior.

XANES was conducted to analyze oxidation states of Fe and Co. Fig. 5a and b demonstrate Co K edge XANES spectra of NH_3-reduced and steam-oxidized $Fe_{0.5}Co_{0.5}O_x$/YSZ at 450 °C and 600 °C, along with standard materials Co, CoO, and Co_3O_4. Comparing the edge energy shifts at the normalized absorption of 0.5 gave that at 450 °C, Co underwent an oxidation state variation of 1.49; whereas at 600 °C, Co underwent a much lower oxidation state change of 0.71, proving that Co

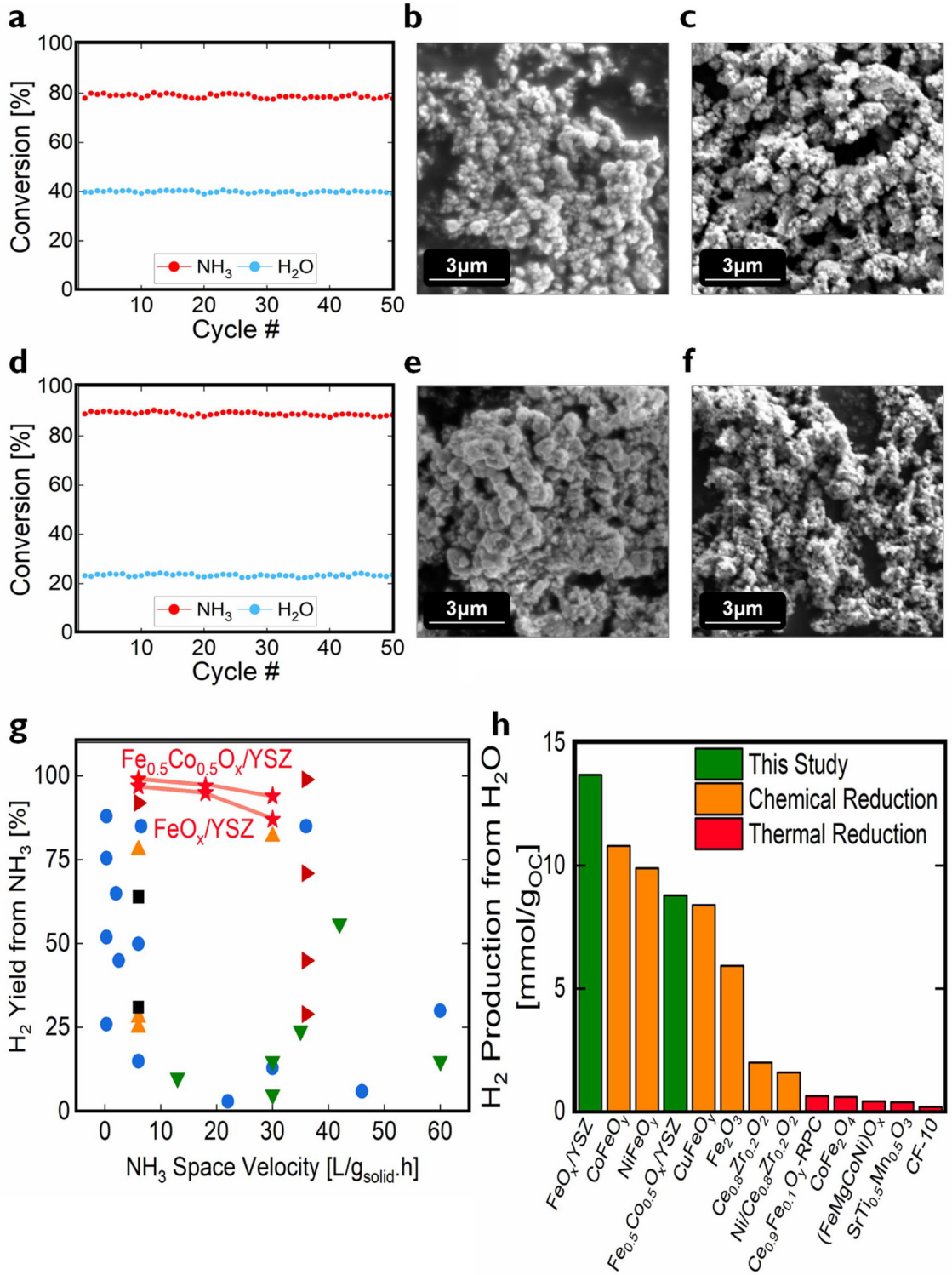

Fig. 3 CLAOD-WS durability and performance comparison with NH_3 decomposition and thermochemical water splitting. (a) 50-cycle NH_3 and H_2O conversions using FeO_x/YSZ at 600 °C, with 30 L_{NH_3} $(g_{solid}\ h)^{-1}$ for 12 min, 12 L_{H_2O} $(g_{solid}\ h)^{-1}$ for 3 min. SEM images of (b) as-synthesized FeO_x/YSZ, and (c) 50-cycled FeO_x/YSZ. (d–f) are $Fe_{0.5}Co_{0.5}O_x$/YSZ results corresponding to (a–c). (g) H_2 yield from NH_3 in our 600 °C CLAOD-WS experiments (red star, only counting H_2 from the NH_3 step), compared to direct decomposition catalysts in literature ranging 450 °C to 700 °C (blue circle: Fe-based,[23,57–69] black square: Co-based,[66,70,71] orange triangle: Ni-based,[72,73] brown triangle: mixed transition metals,[21,22] green triangle: noble metal-based[74–77]). (h) H_2 production in our 600 °C CLAOD-WS experiments (green, only counting H_2 from the H_2O step), compared to thermochemical water splitting in literature (orange: chemical reduction ranging 650 °C to 900 °C,[36,78,79] red: thermal reduction[28–30,33,37,80–82]).

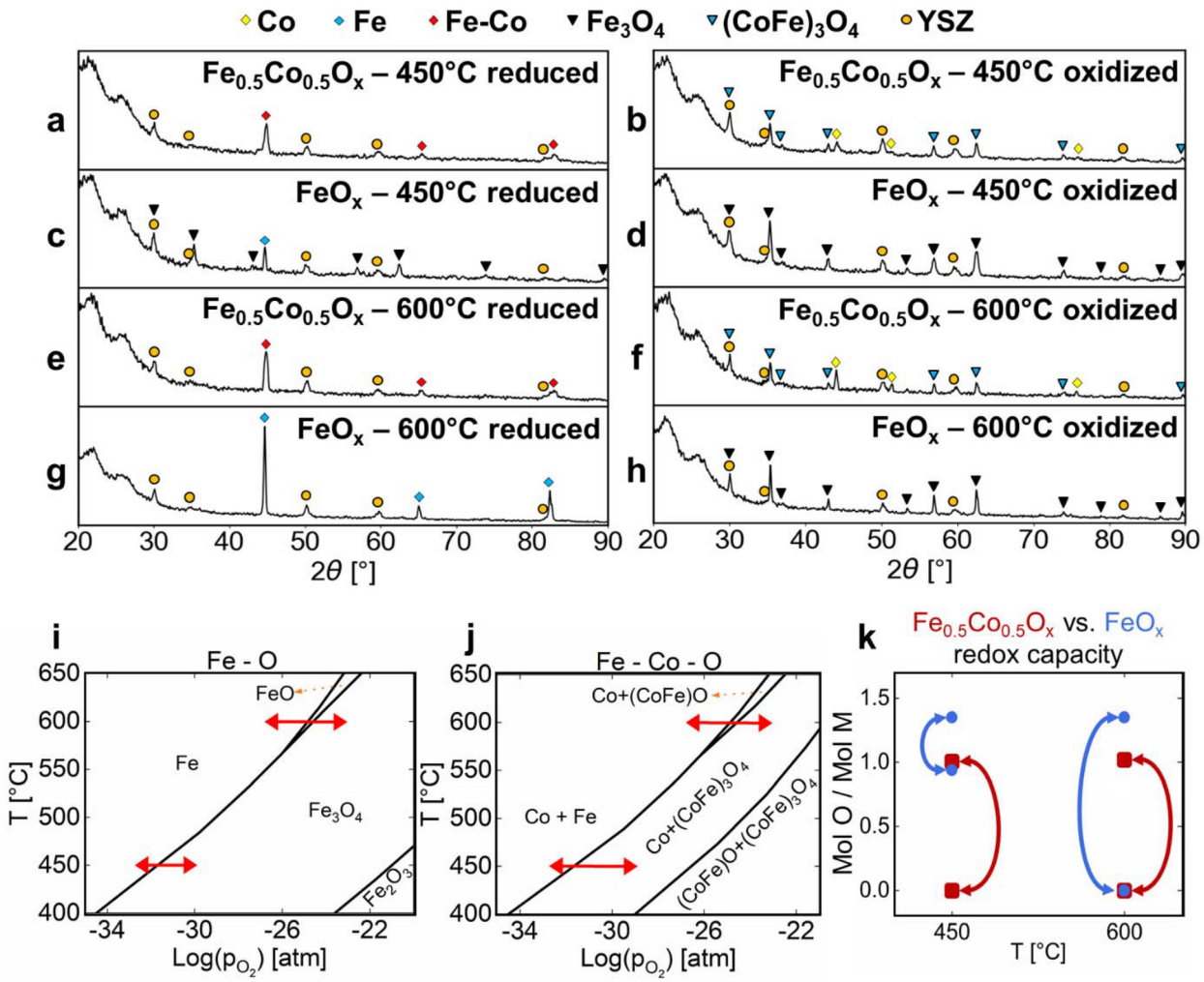

Fig. 4 Solid-state phase transformation of materials for CLAOD-WS. XRD patterns of NH_3-reduced and steam-oxidized samples: (a) reduced $Fe_{0.5}Co_{0.5}O_x$/YSZ, (b) re-oxidized $Fe_{0.5}Co_{0.5}O_x$/YSZ, (c) reduced FeO_x/YSZ, and (d) re-oxidized FeO_x/YSZ at 450 °C; (e–h) are results at 600 °C corresponding to (a–d). (i) Fe–O system, and (j) Fe–Co–O system phase diagrams, where red arrows indicate the equilibrium p_{O_2} ranges between reduced and re-oxidized states according to simulation. (k) Redox ranges of FeO_x/YSZ (blue) and $Fe_{0.5}Co_{0.5}O_x$/YSZ (red) at 450 °C and 600 °C, concluded from XRD refinement.

becomes less redox active at the higher temperature of 600 °C. Fig. 5c and d show the Fe edge XANES results of reduced and re-oxidized $Fe_{0.5}Co_{0.5}O_x$/YSZ along with standard materials of Fe, Fe_3O_4, and $CoFe_2O_4$. We found that at 450 °C Fe underwent a smaller oxidation state variation than at 600 °C. The oxidation state changes of Co and Fe (Tables S2, S3, and S4, and Fig. S6†) were then weight-averaged based on their mole fractions to result in the overall metal redox capacity of $Fe_{0.5}Co_{0.5}O_x$/YSZ at 450 °C and 600 °C in Table 1. Additionally, Fig. 5e and f show the Fe redox of FeO_x/YSZ. The order of overall oxidation state variation in Table 1 agreed with those of water splitting capacity (Fig. 2d) and oxygen capacity derived from XRD phase transformation (Fig. 4k). At 450 °C, $Fe_{0.5}Co_{0.5}O_x$/YSZ is a more redox-active material, while at 600 °C FeO_x/YSZ becomes more redox-active.

As discussed earlier, the materials for CLAOD-WS play the dual-role of oxygen carriers and catalysts. XRD and XANES characterizations of NH_3-reduced and H_2O-oxidized samples illustrate their catalytic activity. For 600 °C experiments, XRD results in Fig. 4e and g show that the FeO_x/YSZ and $Fe_{0.5}Co_{0.5}O_x$/YSZ are fully reduced in NH_3 step to metal phases of Fe and Fe–Co alloy, while the support material YSZ remained unchanged in crystal structure. The XANES experiments (Fig. 5b, d, and f) also show the fully reduced metal phases. Combining the results of XRD and XANES, the metal phases are the active sites for NH_3 decomposition that continues beyond the NH_3 oxidation reaction. High conversions of NH_3 at 600 °C (99% for $Fe_{0.5}Co_{0.5}O_x$/YSZ and 95% for FeO_x/YSZ) show that metal phases are highly catalytically active for NH_3 decomposition at 600 °C. Additionally, we tested as-synthesized and H_2-reduced samples for NH_3 conversion and observed that H_2-reduced samples reach their maximum NH_3 conversion faster than as-synthesized oxides (Fig. S5†), indicating that after reduction of oxides to metal phases, NH_3 conver-

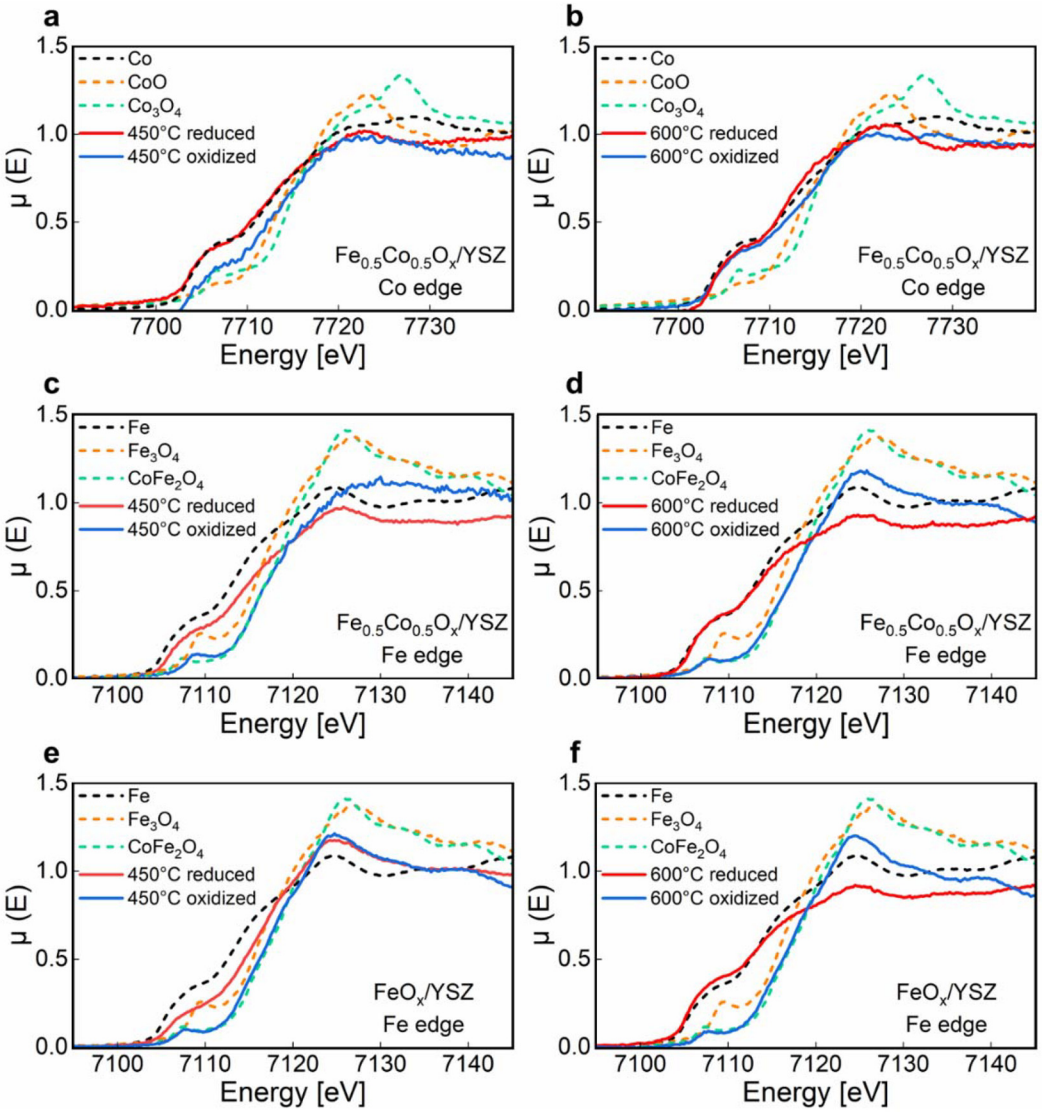

Fig. 5 Simultaneous redox reactions of Fe and Co for CLAOD-WS. XANES results for Co and Fe between NH_3-reduced and steam-oxidized states: Co K edge of $Fe_{0.5}Co_{0.5}O_x$/YSZ at (a) 450 °C and (b) 600 °C, Fe K edge of $Fe_{0.5}Co_{0.5}O_x$/YSZ at (c) 450 °C and (d) 600 °C, and Fe K edge of FeO_x/YSZ at (e) 450 °C and (f) 600 °C.

Table 1 Change in the overall oxidation state of active metals according to XANES

	Overall averaged oxidation state variation per mol of active metals (Fe & Co)	
T [°C]	FeO_x/YSZ	$Fe_{0.5}Co_{0.5}O_x$/YSZ
450	1.31	1.59
600	2.86	1.86

sion is significantly enhanced due to catalytic activity of these active metal sites.

In comparison, at 450 °C, Fig. 4a shows that $Fe_{0.5}Co_{0.5}O_x$/YSZ is fully reduced to Fe–Co metal phase and this phase is responsible for catalytic NH_3 decomposition; however, due to the lower temperature at 450 °C, NH_3 conversion is relatively low (20%). Fig. 4c shows that FeO_x/YSZ is partly reduced to metal Fe phase mixed with Fe_3O_4 spinel phase, resulting in a significantly lower NH_3 conversion of 5% at 450 °C. The XANES experiments for 450 °C samples also agreed with the XRD results. For FeO_x/YSZ, Fig. 5e showed that the oxidation state of Fe is very close to that of Fe_3O_4. For $Fe_{0.5}Co_{0.5}O_x$/YSZ sample, Fig. 5a (Co edge) and Fig. 5c (Fe edge) show that Co and Fe are both reduced to metal phases which are the active phases for NH_3 conversion.

Energy and techno-economic analyses were conducted to assess two systems: (1) Chemical looping ammonia oxidation and decomposition integrated with water splitting (CLAOD-WS) (Fig. 6a), and (2) Catalytic ammonia decompo-

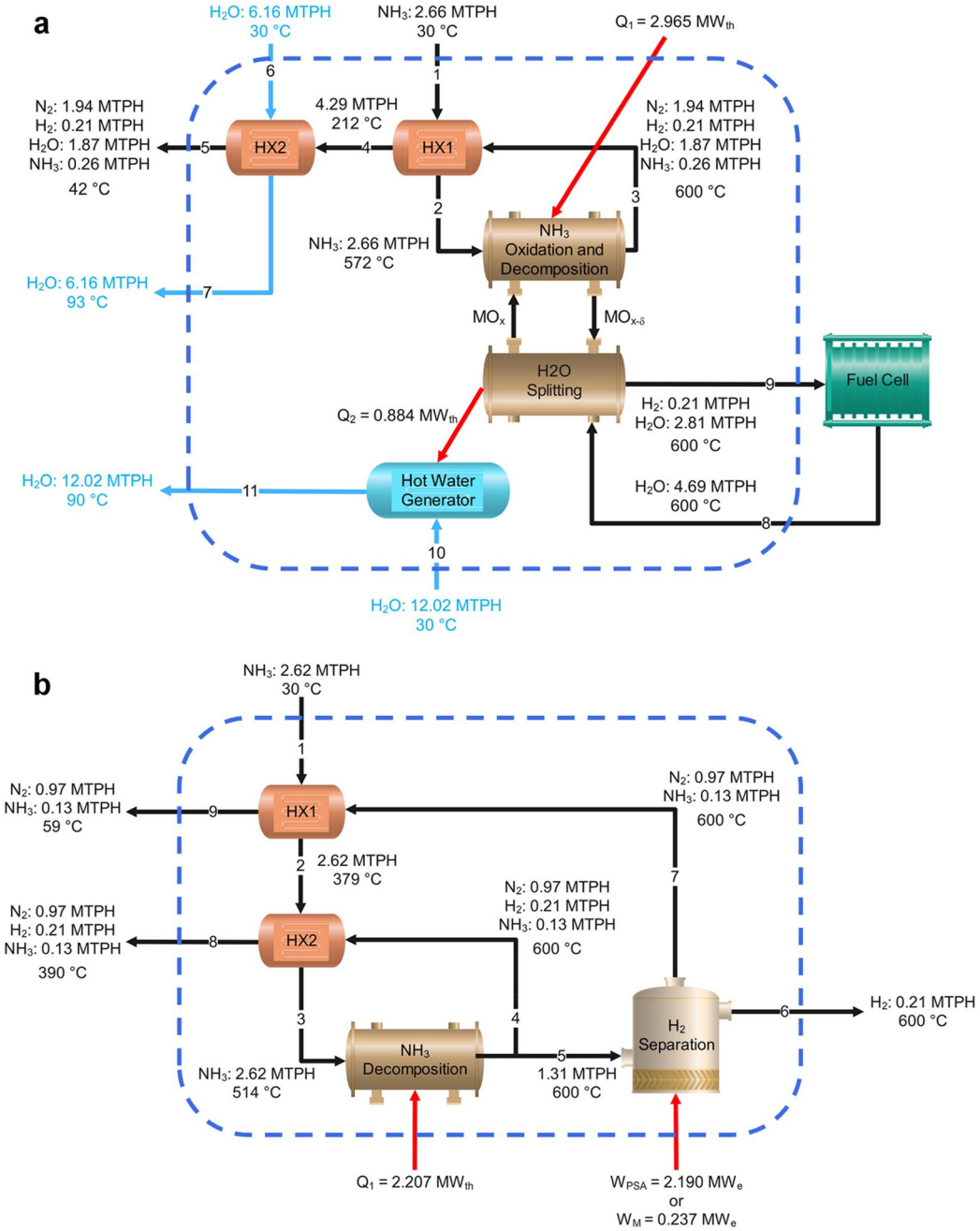

Fig. 6 Process schematics with major model parameters of (a) chemical looping ammonia oxidation and decomposition integrated with water splitting (CLAOD-WS), and (b) catalytic ammonia decomposition (CAD). MTPH: metric ton per hour.

sition (CAD) (Fig. 6b). Major assumptions for both scenarios are: NH_3 conversion is 90%, steam conversion is 40%, reaction temperature is 600 °C, total pressure is 1 atm (except for the PSA where the compressor increases the pressure to 700 kPa), heat exchanger effectiveness is 95%, total H_2 production rate is 10 metric tons per day, and electricity serves as the energy input and is converted to heat when needed and the cost of electricity is assumed to be \$0.053 per kWh_e (following utility-scale PV-plus-battery system, class 5, moderate case, market, PTC + ITC, 2030).[83] For CLAOD-WS, 5 tons per day of H_2 comes out of each of NH_3 reaction and steam reaction. For CAD, 5 tons per day of H_2 is purified in the separation step, where two types of H_2 separation technologies were analyzed: PSA and Pd-Ag membrane supported on ceramic material. Base case membrane separation has a Second Law efficiency of 20%. The redox or catalyst material is assumed to be replaced 4 times

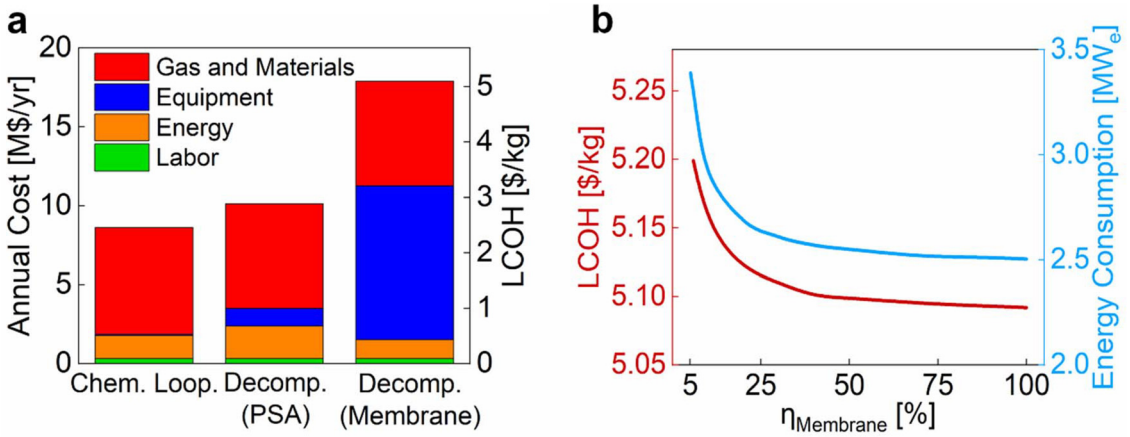

Fig. 7 (a) Annual cost and levelized cost of hydrogen (LCOH) for CLAOD-WS and for CAD equipped with pressure swing absorption (PSA) or Pd-Ag/ceramic membrane separation. (b) Dependence of LCOH and total system energy consumption rate on H_2 separation membrane Second Law efficiency in CAD process with Pd-Ag/ceramic membrane separation.

per year,[84] and we find that the replacement frequency varying from once per year to once per two weeks only changes LCOH by less than 2% for all cases in this work.

In CLAOD-WS, the NH_3 step is the main thermal energy consumer (2.965 MW_{th}). In CAD, although the chemical reactor is less energy intensive (2.207 MW_{th}), the H_2 separation requires an energy input of 0.237 MW_e for the membrane and 2.190 MW_e for the PSA. Overall, the CLAOD-WS system is 22.5% more energy-consuming than the membrane-based CAD system and 29.1% less energy-consuming than the PSA-based CAD system.

As Fig. 7a shows, notably, CLAOD-WS process achieves cost savings of 52% and 86% in energy and equipment expenses compared to CAD plants utilizing PSA and membrane systems, respectively. The CLAOD-WS plant requires an annual cost of $8.64 M, 51.8% lower than the CAD plant equipped with membrane separation and 14.8% lower than the CAD plant equipped with PSA separation. Accordingly, the LCOH is $2.5 per kg-$H_2$ in CLAOD-WS, $5.1 per kg-$H_2$ in CAD with membrane, and $2.9 per kg-$H_2$ in CAD with PSA. LCOH refers to the cost per kilogram of H_2 production from both NH_3 and H_2O steps in CLAOD-WS. In addition, thermal energy release in CLAOD-WS can be used to produce hot water byproduct, whose revenue is not included in our economic analysis. Fig. 7b compares the LCOH and total energy consumption rate in the CAD as a function of the membrane's H_2 separation Second Law efficiency, showing the impact of membrane performance.

4. Conclusions

We have proposed and studied integrated chemical looping NH_3 oxidation and decomposition with water splitting (CLAOD-WS) as a promising novel pathway toward H_2 production from NH_3 and H_2O. FeO_x/YSZ and $Fe_{0.5}Co_{0.5}O_x$/YSZ each played the dual roles of oxygen carrier and catalyst. Looping experiments at 450 to 600 °C and space velocities of 6, 18, and 30 L_{NH_3} $(g_{solid}\ h)^{-1}$ and 12 L_{H_2O} $(g_{solid}\ h)^{-1}$ were conducted. XRD coupled with phase diagrams illustrated that FeO_x/YSZ is kinetically limited from achieving full reduction at 450 °C, while $Fe_{0.5}Co_{0.5}O_x$/YSZ is thermodynamically limited from complete oxidation under H_2O. Moreover, XRD refinements and XANES results showed the Fe and Co redox activities that explain the overall redox capacity of $Fe_{0.5}Co_{0.5}O_x$/YSZ and FeO_x/YSZ at different temperatures, consistent with the experimental water splitting capacity. Durability of the materials was shown by 50-cycle CLAOD-WS experiments at 600 °C and 30 L_{NH_3} $(g_{solid}\ h)^{-1}$. Lastly, energy and techno-economic analysis of the CLAOD-WS and catalytic NH_3 decomposition systems indicated that the looping scheme can significantly reduce energy consumption and cost mainly due to the intrinsic H_2 purification in the looping scheme.

Data availability

Further information on materials and code used in the work are available from the lead contact upon reasonable request. Crystallographic data used for XRD data analysis has been deposited at the ICSD and can be obtained from **https://icsd.products.fiz-karlsruhe.de/en**. Additional data used in this study is available in the ESI.†

Conflicts of interest

The authors declare no competing financial interest.

Acknowledgements

The authors acknowledge Center for Electron Microscopy and Analysis (CEMAS) and Surface Analysis Laboratory at The Ohio

State University (OSU). The research is partly supported by OSU President's Research Excellence Program. A. Arjomand is partly supported by US Department of Energy DE-EE0010733. K. Shank is supported by Distinguished University Fellowship and ENGIE-Axium Fellowship at OSU.

References

1 S. Ristig, M. Poschmann, J. Folke, O. Gómez-Cápiro, Z. Chen, N. Sanchez-Bastardo, R. Schlögl, S. Heumann and H. Ruland, *Chem. Ing. Tech.*, 2022, **94**, 1413–1425.
2 B. Modu, M. P. Abdullah, A. L. Bukar and M. F. Hamza, *Int. J. Hydrogen Energy*, 2023, **48**, 38354–38373.
3 A. Arjomand Kermani and E. Houshfar, *Int. J. Hydrogen Energy*, 2024, **52**, 177–189.
4 I. Lucentini, X. Garcia, X. Vendrell and J. Llorca, *Ind. Eng. Chem. Res.*, 2021, 18560–18611.
5 A. Pal, S. Kakran, A. Kumar, A. B. Youssef, U. P. Singh and A. Sidhu, *Int. J. Hydrogen Energy*, 2024, **49**, 16–41.
6 M. Koleva and N. Rustagi, *Hydrogen Delivery and Dispensing Cost – DOE Hydrogen and Fuel Cells Program Record*.
7 J. W. Sheffield, K. B. Martin and R. Folkson, in *Alternative Fuels and Advanced Vehicle Technologies for Improved Environmental Performance*, ed. R. Folkson, Woodhead Publishing, 2014, pp. 117–137.
8 Physical Hydrogen Storage – Hydrogen and Fuel Cell Technologies Office, **https://energy.gov/eere/fuelcells/physical-hydrogen-storage**.
9 L. Mulky, S. Srivastava, T. Lakshmi, E. R. Sandadi, S. Gour, N. A. Thomas, S. Shanmuga Priya and K. Sudhakar, *Mater. Chem. Phys.*, 2024, **325**, 129710.
10 F. Dawood, M. Anda and G. M. Shafiullah, *Int. J. Hydrogen Energy*, 2020, **45**, 3847–3869.
11 M. F. Platzer and N. Sarigul-Klijn, in *The Green Energy Ship Concept: Renewable Energy from Wind Over Water*, ed. M. F. Platzer and N. Sarigul-Klijn, Springer International Publishing, Cham, 2021, pp. 71–72.
12 A. Valera-Medina, H. Xiao, M. Owen-Jones, W. I. F. David and P. J. Bowen, *Prog. Energy Combust. Sci.*, 2018, **69**, 63–102.
13 A. Roy, S. Sen Gupta, A. Samanta, P. V. S. Sai Likhith and S. K. Das, *Int. J. Hydrogen Energy*, 2024, **71**, 131–142.
14 N. Othman, H. Salleh and H. Purwanto, *Procedia Chem.*, 2016, 119–124.
15 R. Lan, J. T. S. Irvine and S. Tao, *Int. J. Hydrogen Energy*, 2012, **37**, 1482–1494.
16 J. Bartels, *A Feasibility Study of Implementing an Ammonia Economy*, Iowa State University, 2008.
17 L. Zhai, S. Liu and Z. Xiang, *Ind. Chem. Mater.*, 2023, **1**, 332–342.
18 O. Ojelade and S. Zaman, *Chem. Pap.*, 2020, 57–65.
19 F. Schuth, R. Palkovits, R. Schlogl and D. S. Su, *Energy Environ. Sci.*, 2011, 6278–6289.
20 Z. Hu, C. Weng, C. Chen and Z. Yuan, *Appl. Catal., A*, 2018, 49–57.
21 H. Tabassum, S. Mukherjee, J. Chen, D. Holiharimanana, S. Karakalos, X. Yang, S. Hwang, T. Zhang, B. Lu, M. Chen, Z. Tang, E. A. Kyriakidou, Q. Ge and G. Wu, *Energy Environ. Sci.*, 2022, **15**, 4190–4200.
22 P. Xie, Y. Yao, Z. Huang, Z. Liu, J. Zhang, T. Li, G. Wang, R. Shahbazian-Yassar, L. Hu and C. Wang, *Nat. Commun.*, 2019, **10**, 4011.
23 Y.-Q. Gu, Z. Jin, H. Zhang, R.-J. Xu, M.-J. Zheng, Y.-M. Guo, Q.-S. Song and C.-J. Jia, *J. Mater. Chem. A*, 2015, **3**, 17172–17180.
24 L. Yao, T. Shi, Y. Li, J. Zhao, W. Ji and C.-T. Au, *Catal. Today*, 2011, **164**, 112–118.
25 F. Normann, A. O. Wismer, C. R. Müller and H. Leion, *Fuel*, 2019, 57–63.
26 M. Cheng, F. Normann, D. Zhao, Z. Li, N. Cai and H. Leion, *Energy Fuels*, 2015, 8126–8134.
27 C. Ruan, X. Wang, C. Wang, L. Zheng, L. Li, J. Lin, X. Liu, F. Li and X. Wang, *Nat. Commun.*, 2022, 1–12.
28 S. Zhai, J. Rojas, N. Ahlborg, K. Lim, M. F. Toney, H. Jin, W. C. Chueh and A. Majumdar, *Energy Environ. Sci.*, 2018, 2172–2178.
29 X. Qian, J. He, E. Mastronardo, B. Baldassarri, C. Wolverton and S. M. Haile, *Chem. Mater.*, 2020, **32**, 9335–9346.
30 Y. Mao, Y. Gao, W. Dong, H. Wu, Z. Song, X. Zhao, J. Sun and W. Wang, *Appl. Energy*, 2020, **267**, 114860.
31 A. Pérez, M. Orfila, M. Linares, R. Sanz, J. Marugán, R. Molina and J. A. Botas, *Catal. Today*, 2022, **390–391**, 22–33.
32 X. Li, X. Sun, Q. Song, Z. Yang, H. Wang and Y. Duan, *Int. J. Hydrogen Energy*, 2022, **47**, 33619–33642.
33 C. Bu, T. Gu, S. Cen, D. Liu, J. Meng, C. Liu, X. Wang, H. Xie, J. Zhang and G. Piao, *Int. J. Hydrogen Energy*, 2023, **48**, 12227–12239.
34 V. K. Budama, J. P. Rincon Duarte, M. Roeb and C. Sattler, *Sol. Energy*, 2023, **249**, 353–366.
35 B. Ghorbani, S. Zendehboudi, Y. Zhang, H. Zarrin and I. Chatzis, *Energy Convers. Manage.*, 2023, **297**, 117599.
36 Y. Liu, T. Gu, C. Bu, D. Liu and G. Piao, *Int. J. Hydrogen Energy*, 2024, **62**, 1077–1088.
37 A. M. Huerta-Flores, F. Torre, M. Taeño, R. C. Barreno, E. Palomo Del Barrio and S. Doppiu, *Int. J. Hydrogen Energy*, 2024, **71**, 1293–1302.
38 J. T. Tran, K. J. Warren, D. Mejic, R. L. Anderson, L. Jones, D. S. Hauschulz, C. Wilson and A. W. Weimer, *Joule*, 2023, **7**, 1759–1768.
39 E. Gager, M. Frye, D. McCord, J. Scheffe and J. C. Nino, *Int. J. Hydrogen Energy*, 2022, **47**, 31152–31164.
40 D. Zhang, H. A. De Santiago, B. Xu, C. Liu, J. A. Trindell, W. Li, J. Park, M. A. Rodriguez, E. N. Coker, J. D. Sugar, A. H. McDaniel, S. Lany, L. Ma, Y. Wang, G. Collins, H. Tian, W. Li, Y. Qi, X. Liu and J. Luo, *Chem. Mater.*, 2023, **35**, 1901–1915.
41 G. L. Schieber, E. B. Stechel, A. Ambrosini, J. E. Miller and P. G. Loutzenhiser, *Int. J. Hydrogen Energy*, 2017, **42**, 18785–18793.

42 B. Bulfin, M. Miranda and A. Steinfeld, *Front. Energy Res.*, 2021, **9**, 677980.
43 R. B. Wexler, G. Sai Gautam, R. T. Bell, S. Shulda, N. A. Strange, J. A. Trindell, J. D. Sugar, E. Nygren, S. Sainio, A. H. McDaniel, D. Ginley, E. A. Carter and E. B. Stechel, *Energy Environ. Sci.*, 2023, **16**, 2550–2560.
44 H. N. N. Tran, W. Li and X. Liu, *Chem. Eng. J.*, 2024, **500**, 156613.
45 L.-S. Fan and F. Li, *Ind. Eng. Chem. Res.*, 2010, **49**, 10200–10211.
46 L.-S. Fan, *Chemical looping partial oxidation: gasification, reforming, and chemical syntheses*, Cambridge University Press, 2017.
47 X. Zhu, Q. Imtiaz, F. Donat, C. R. Müller and F. Li, *Energy Environ. Sci.*, 2020, **13**, 772–804.
48 Z. Du, C. Liu, J. Zhai, X. Guo, Y. Xiong, W. Su and G. He, *Catalysts*, 2021, **11**, 393.
49 I. Staffell, D. Scamman, A. Velazquez Abad, P. Balcombe, P. E. Dodds, P. Ekins, N. Shah and K. R. Ward, *Energy Environ. Sci.*, 2019, **12**, 463–491.
50 K. Wróbel, J. Wróbel, W. Tokarz, J. Lach, K. Podsadni and A. Czerwiński, *Energies*, 2022, **15**, 8937.
51 S. Yun, J. Im, J. Kim, H. Cho and J. Lee, *Chem. Eng. J.*, 2024, **491**, 151875.
52 M. Nordio, S. A. Wassie, M. Van Sint Annaland, D. A. Pacheco Tanaka, J. L. Viviente Sole and F. Gallucci, *Int. J. Hydrogen Energy*, 2021, **46**, 23417–23435.
53 C. Makhloufi and N. Kezibri, *Int. J. Hydrogen Energy*, 2021, **46**, 34777–34787.
54 S. Devkota, J.-Y. Cha, B.-J. Shin, J.-H. Mun, H. C. Yoon, S. A. Mazari and J.-H. Moon, *Appl. Energy*, 2024, **358**, 122605.
55 B. Ravel and M. Newville, *J. Synchrotron Radiat.*, 2005, **12**, 537–541.
56 H. F. Rase and J. R. Holmes, *Chemical reactor design for process plants*, Wiley, New York, 1977.
57 X. Duan, G. Qian, X. Zhou, Z. Sui, D. Chen and W. Yuan, *Appl. Catal., B*, 2011, **101**, 189–196.
58 A.-H. Lu, J.-J. Nitz, M. Comotti, C. Weidenthaler, K. Schlichte, C. W. Lehmann, O. Terasaki and F. Schüth, *J. Am. Chem. Soc.*, 2010, **132**, 14152–14162.
59 M. Itoh, M. Masuda and K.-I. Machida, *Mater. Trans.*, 2002, **43**, 2763–2767.
60 T. Otremba, N. Frenzel, M. Lerch, T. Ressler and R. Schomäcker, *Appl. Catal., A*, 2011, **392**, 103–110.
61 Z.-P. Hu, L. Chen, C. Chen and Z.-Y. Yuan, *Mol. Catal.*, 2018, **455**, 14–22.
62 X.-C. Hu, W.-W. Wang, Z. Jin, X. Wang, R. Si and C.-J. Jia, *J. Energy Chem.*, 2019, **38**, 41–49.
63 H. Tüysüz, F. Schüth, L. Zhi, K. Müllen and M. Comotti, *ChemCatChem*, 2015, **7**, 1453–1459.
64 B. Lorenzut, T. Montini, M. Bevilacqua and P. Fornasiero, *Appl. Catal., B*, 2012, **125**, 409–417.
65 W. Arabczyk and J. Zamlynny, *Catal. Lett.*, 1999, **60**, 167–171.
66 H. Zhang, Y. A. Alhamed, Y. Kojima, A. A. Al-Zahrani and L. A. Petrov, *Proceedings of the Bulgarian Academy of Sciences*, 2013, 519–524.
67 K. F. Ortega, D. Rein, C. Lüttmann, J. Heese, F. Özcan, M. Heidelmann, J. Folke, K. Kähler, R. Schlögl and M. Behrens, *ChemCatChem*, 2017, **9**, 659–671.
68 L. Li, Q. Meng, W. Ji, J. Shao, Q. Xu and J. Yan, *Mol. Catal.*, 2017, **442**, 147–153.
69 Y. Yuan, *Science*, 2022, 889–893.
70 C. Huang, Y. Yu, X. Tang, Z. Liu, J. Zhang, C. Ye, Y. Ye and R. Zhang, *Appl. Surf. Sci.*, 2020, **532**, 147335.
71 S. Podila, H. Driss, S. F. Zaman, Y. A. Alhamed, A. A. AlZahrani, M. A. Daous and L. A. Petrov, *J. Mol. Catal. A: Chem.*, 2016, **414**, 130–139.
72 K. Okura, K. Miyazaki, H. Muroyama, T. Matsui and K. Eguchi, *RSC Adv.*, 2018, **8**, 32102–32110.
73 H. Liu, H. Wang, J. Shen, Y. Sun and Z. Liu, *Appl. Catal., A*, 2008, **337**, 138–147.
74 S.-F. Yin, B.-Q. Xu, C.-F. Ng and C.-T. Au, *Appl. Catal., B*, 2004, **48**, 237–241.
75 P. F. Ng, L. Li, S. Wang, Z. Zhu, G. Lu and Z. Yan, *Environ. Sci. Technol.*, 2007, 3758–3762.
76 R. Antunes, R. Steiner, L. Marot and E. Meyer, *Int. J. Hydrogen Energy*, 2022, **47**, 14130–14140.
77 B. Bahrami, V. G. Komvokis, M. S. Ziebarth, O. S. Alexeev and M. D. Amiridis, *Appl. Catal., B*, 2013, **130–131**, 25–35.
78 Y. Qiu, S. Zhang, D. Cui, M. Li, J. Zeng, D. Zeng and R. Xiao, *Appl. Energy*, 2019, **252**, 113454.
79 Y. Zheng, K. Li, H. Wang, X. Zhu, Y. Wei, M. Zheng and Y. Wang, *Energy Fuels*, 2016, **30**, 638–647.
80 K. Zheng, Z. Yu, S.-C. Tan, T. Liu and H. Kong, *Energy Convers. Manage.*, 2024, **303**, 118116.
81 A. Haeussler, S. Abanades, A. Julbe, J. Jouannaux, M. Drobek, A. Ayral and B. Cartoixa, *Chem. Eng. Res. Des.*, 2020, **156**, 311–323.
82 M. Orfila, D. Sanz, M. Linares, R. Molina, R. Sanz, J. Marugán and J.Á Botas, *Int. J. Hydrogen Energy*, 2021, **46**, 17458–17471.
83 Annual Technology Baseline – Utility Scale PV plus Battery, **https://atb.nrel.gov/electricity/2024/utility-scale_pv-plus-battery**.
84 S. Zhai, *Iron-based Oxides for Thermochemical Splitting of Water and Carbon Dioxide*, Stanford University, 2020.